# A Fast Spectral Line-Ratio Algorithm for Mesospheric Airglow Rotational Temperature Retrieval and Validation

Shuqi Niu [1], Shengyang Gu[1,2], Haiyang Gao[3], Dini Gong[1], Yafei Wei[1], Yusong Qin[1]

[1] School of Earth and Space Science and Technology, Wuhan University, Wuhan 430072, China

[2]Wuhan Institute of Quantum Technology, Wuhan, 430072, China

[3]State Key Laboratory of Environment Characteristics and Effects for Near-space, Nanjing University of Information Science and Technology, Nanjing 210044, China

*Correspondence to*: Shengyang Gu (gushengyang@whu.edu.cn)

**Abstract.** Airglow rotational temperatures are effective tracers of variability in the mesopause region. To improve computational efficiency in processing long-duration, high-temporal-resolution observations from the Mesospheric Airglow Spectrum Photometer (MASP), a Fast Airglow Spectral Line-Ratio algorithm (FASLR) is developed for rotational temperature retrieval. FASLR uses forward-modeled synthetic spectra to establish ratio–temperature relationships, derives independent temperature estimates from multiple line-intensity ratios, and combines them with weights based on the relative sensitivity of each ratio to instrumental perturbations. For the two test nights containing 132 and 120 observations, the complete FASLR processing required 19.0 and 16.8 s, respectively. FASLR temperatures are compared with two nights of co-located sodium fluorescence Doppler lidar observations. The major nocturnal temperature variations are generally similar between the two measurements, while differences in their absolute temperature levels are also observed. The algorithm is then applied to six nights of dual-channel MASP observations of the $O_2$ (0–1) and OH (6–2) emissions and compared with independent satellite observations from SABER and Aura/MLS, as well as temperature estimates from SD-WACCMX and NRLMSIS 2.1. At representative emission-layer altitudes, the $O_2$ rotational temperatures are generally closer to NRLMSIS 2.1 in overall temperature level, although their nocturnal variations differ. The OH temperatures are higher than NRLMSIS 2.1 early in the night but become closer later. SD-WACCMX generally gives lower temperatures and weaker nocturnal variability in both emission layers. Case studies further show longer-period nocturnal variability and shorter-period disturbances in the FASLR-derived temperatures. On 2 February 2024, temperature and intensity perturbations in the $O_2$ and OH layers exhibit a common

dominant period band and stable phase relationships. On 7 February 2024, both layers show concurrent power enhancements within a similar period band, and simultaneous observations from the Mesospheric Airglow Wide-angle Imager (MAWI) independently support the identified disturbance. Overall, FASLR provides an efficient approach for dual-channel airglow temperature retrieval and supports investigations of wave-related variability in the mesopause region.

**Keywords** Temperature retrieval, Airglow Spectrum Photometer, Spectral line ratio, Dual-channel airglow observations, Data comparison, Gravity waves

## 1.Introduction

The mesosphere and lower thermosphere (MLT, ~50–120 km) constitute a key transition region between the lower atmosphere and the thermosphere–ionosphere system. Within the MLT, the mesopause region is of particular importance. Its temperature is a key parameter for characterizing multiscale dynamical processes and associated energy transfer, and for assessing long-term changes in the upper atmosphere in a changing climate (Li et al., 2010; Wan and Xu, 2014; Yue et al., 2015; Chen et al., 2016; Yi et al., 2023). However, the thermal structure of the mesopause region exhibits pronounced spatiotemporal variability, and single-point observations are often insufficient to capture both its regional structure and temporal evolution. Coordinated multi-instrument observations and observational networks can provide continuous temporal coverage and spatial context, thereby supporting studies of large-scale circulation, wave propagation, and coupling between atmospheric layers (Shepherd et al., 2020; Stober et al., 2021; Wang et al., 2022; Yang et al., 2024).

Among the available approaches, passive optical remote sensing is particularly well suited for temperature observations in the mesopause region. Nocturnal airglow emissions, such as $O_2$ and OH, contain rotational spectral features whose line intensities and intensity ratios can be used to retrieve rotational temperature (Sargoytchev et al., 2004; French et al., 2020; Wüst et al., 2023). Airglow spectrometers are relatively simple, operationally stable, and well suited for long-term continuous operation, and they have been deployed in observational networks to support regional temperature comparisons and variability studies (Shepherd et al., 2002; Reisin et al., 2014; Xu et al., 2015). In China, temperature retrieval methods based on OH and $O_2$ rotational spectra have also been explored (Xiong et al., 2012; Liu et al., 2015), showing the potential of this approach for broader deployment in observational networks. Continuous MLT airglow observations provide valuable information on

temporal variability. Efficient and reliable data processing and temperature retrieval are therefore important for making full use of these measurements, particularly in studies of short-term temperature variability, wave dynamics, and model evaluation. To process continuous airglow observations with high temporal resolution, temperature retrieval methods need to balance computational cost, accuracy, and stability. Early approaches often relied on a limited number of rotational lines or line-intensity ratios to estimate temperature (Takeuchi and Misawa, 1979; Takeuchi et al., 1979). These methods are conceptually straightforward and require only limited spectral information, but they can be sensitive to variations in signal-to-noise ratio (SNR), background contamination, and uncertainties in line-intensity parameters. Subsequently, multi-line approaches based on Boltzmann-plot regression of several rotational transitions were increasingly adopted for rotational temperature retrieval and reduced the dependence on individual spectral lines (Sigernes et al., 2003; Mulligan et al., 2009). Advances in instrumentation and high-resolution spectroscopy, together with improved spectroscopic data for OH transitions, have further improved the accuracy and reliability of airglow temperature retrievals (Osterbrock et al., 1996; Brooke et al., 2016; Noll et al., 2023). However, the cost of instrumentation and the associated observational requirements can constrain broader use of these approaches in long-term and networked observations. More recently, optimal-estimation frameworks have also been explored in airglow remote sensing, allowing the incorporation of a priori constraints and a more rigorous characterization of posterior uncertainty (Sun et al., 2022). Such approaches involve more complex retrieval procedures than simpler methods based on line-intensity ratios.

A multi-parameter iterative inversion algorithm (MPII) was previously developed for the Mesospheric Airglow Spectrum Photometer (MASP). In MPII, instrumental parameters are adjusted iteratively together with the forward spectral calculation to reproduce each observed spectrum and retrieve rotational temperature. Temperatures retrieved with MPII have also been compared with coordinated sodium fluorescence Doppler lidar observations (Niu et al., 2024). Because each retrieval involves iterative parameter adjustment and repeated forward-model evaluations, computational efficiency becomes an important consideration when processing continuous, high-temporal-resolution observations.

In this study, a fast rotational temperature retrieval algorithm based on airglow line-intensity ratios is developed to provide a direct, non-iterative approach. The algorithm establishes ratio–temperature relationships using a forward model and combines multiple ratio-based temperature estimates using weights based on their sensitivities to instrumental-parameter perturbations.

The resulting retrieval does not require per-spectrum iterative optimization, reducing the computational cost of processing continuous observations. It is applied here to dual-channel MASP observations to investigate nocturnal temperature variations and wave signatures in the mesopause region.

## 2. Instrumentation and Datasets

### 2.1 MASP instrument and observation configurations

MASP is a zenith-viewing airglow spectrum photometer with a field of view of 12.9°. The instrument was operated in two configurations for the observations analyzed in this study. In the original single-channel configuration, MASP continuously measured the $O_2$ (0–1) airglow emission, providing a temporal resolution of 3 min. In the dual-channel configuration, a filter wheel was added to enable alternating measurements of the $O_2$ (0–1) and OH (6–2) emissions. The exposure times were 3 min for $O_2$ and 2 min for OH, and successive measurements of each emission band were separated by approximately 5.3 min. The effective temporal resolution of each retrieved temperature series was therefore approximately 5.3 min.

Representative emission heights of 94 and 87 km are adopted for the $O_2$ and OH airglow layers, respectively. Both interference filters have an aperture of 50 mm. Their center wavelengths are 867.1 nm for $O_2$ and 837.17 nm for OH, with corresponding bandwidths of 0.24 and 0.26 nm. Further details of the MASP optical design and its original single-channel configuration are provided by Niu et al. (2024).

### 2.2 Observations and datasets

#### 2.2.1 MASP observation datasets

Two MASP observation datasets are used in this study. The first was obtained during coordinated observations of MASP and a sodium fluorescence Doppler lidar at the National Space Science Center, Chinese Academy of Sciences, in Huairou, Beijing (40°N, 116°E), in 2023. MASP was operated in the single-channel configuration described in Sect. 2.1, providing an $O_2$ rotational-temperature series with a temporal resolution of 3 min. Two nights with high-quality simultaneous observations, 26

April and 23 May 2023, were selected for comparisons among FASLR, MPII, and sodium fluorescence Doppler lidar temperatures.

The second dataset was obtained at the Tulihe Meteorological Observatory, Hulunbuir, Inner Mongolia (50.5°N, 122.6°E; Fig. 1), from 2 to 7 February 2024. MASP was operated in the alternating dual-channel configuration described in Sect. 2.1, providing $O_2$ and OH rotational-temperature series with an effective temporal resolution of approximately 5.3 min for each channel. This dataset was used for dual-channel temperature retrievals, comparisons with satellite and model temperatures, and analyses of nocturnal variability and wave disturbances.




**Figure 1: Photograph of the observation setup at Tulihe, together with representative MASP dual-channel airglow images in the $O_2$ (0–1) and OH (6–2) bands and a representative MAWI image.**

### 2.2.2 Sodium fluorescence Doppler lidar data

The lidar provides temperature profiles over 75–105 km with a temporal resolution of 10 min and a vertical resolution of 1 km. For comparison with the MASP $O_2$ rotational temperatures, the lidar temperature profiles were weighted and averaged over 92–96 km to obtain a layer-representative temperature for the MASP $O_2$ emission layer. Both the MASP and lidar datasets

were retained at their original temporal resolutions. In this study, the lidar temperatures are used for independent comparison with the FASLR-derived temperatures.

### 2.2.3 Auxiliary datasets

Satellite observations from SABER and Aura/MLS and temperature estimates from SD-WACCMX and NRLMSIS 2.1 are used for observational and model-based comparisons with the dual-channel MASP temperatures, respectively. Simultaneous MAWI observations are additionally used to examine wave-related disturbances. All datasets are converted to China local time (LTC, UTC+8) to ensure a consistent time reference.

Satellite temperature profiles are obtained from SABER and Aura/MLS during 2–7 February 2024. For comparison with the MASP observations, only satellite overpasses occurring within the MASP observation intervals are used, although orbital constraints usually limit the number of samples to one or two per night. Overpasses within a ±20° latitude and ±20° longitude window centered on the observation site (50.5°N, 122.6°E) are selected. To approximate the airglow emission layers, the satellite profiles are vertically averaged using altitude-dependent weights over 85–89 km for OH and 92–96 km for $O_2$, yielding representative layer temperatures.

Temperature estimates from SD-WACCMX and NRLMSIS 2.1 are extracted near the observation site and calculated over fixed altitude ranges of 85–89 km for OH and 92–96 km for $O_2$. The SD-WACCMX profiles are interpolated to fixed altitude levels to ensure consistent vertical sampling. The NRLMSIS 2.1 temperatures are calculated directly at the same fixed altitude levels. To characterize the nighttime background temperature level and mean nocturnal evolution, the six-night temperature time series are aligned to a common LTC axis and averaged point by point to construct mean nocturnal temperature curves. These curves are then compared with the corresponding mean variations in the MASP observations.

In addition, data from the Mesospheric Airglow Wide-angle Imager (MAWI), acquired simultaneously with MASP, are used to examine transient disturbances (Fig. 1). The imager covers 750–850 nm, with an exposure time of 3 min, a cadence of 6.8 min, and a field of view of 120°. After standard image preprocessing (Huang et al., 2025), the resulting wave-like band structures are compared with transient features identified in the MASP wavelet analysis in terms of their occurrence time and morphology.

### 3. Fast Airglow Spectral Line-Ratio Algorithm（FASLR）

#### 3.1 Physical basis

Under near-local thermodynamic equilibrium (LTE), the relative intensities of rotational lines within a given vibrational band vary systematically with rotational temperature and can therefore be used to retrieve rotational temperature (Mies, 1974). For OH airglow, the applicability and limitations of this approach, including possible non-LTE effects, have been discussed by Noll et al. (2016). For optically thin airglow emissions, the intensity of an individual rotational line depends primarily on the population of the corresponding upper rotational level, as well as on line-specific molecular parameters and the instrumental spectral response. Forming line-intensity ratios can reduce common instrumental effects, but cannot fully remove line-dependent instrumental responses or the unequal sensitivities of different ratios to instrumental-parameter variations. The resulting ratios therefore depend mainly on rotational temperature and known line-specific constants, but they retain different sensitivities to instrumental perturbations. For the $O_2$ (0–1) airglow emission, whose peak altitude is near 94 km, the lower rotational levels are commonly assumed to be close to LTE. The retrieved rotational temperature can therefore be treated as a reasonable approximation of the ambient kinetic temperature (Mies, 1974). Under this assumption, the rotational temperature derived from a selected line pair can be expressed as:

$$T_{n,m}=\frac{E_{v'}\left(J'_m\right)-E_{v'}\left(J'_n\right)}{k\,ln\left[\frac{I_n}{I_m}\frac{A\left(J'_m,v'\rightarrow J''_{m+1},v''\right)}{A\left(J'_n,v'\rightarrow J''_{n+1},v''\right)}\frac{2J'_m+1}{2J'_n+1}\right]}, \tag{1}$$

where $T_{n,m}$ is the rotational temperature derived from lines $n$ and $m$, $I_n$ and $I_m$ are the corresponding line intensities, $J'_n$ *and* $J'_m$ are the upper-state rotational quantum numbers, $E_{v'}(J')$ is the upper-level energy, and $A$ denotes the Einstein $A$ coefficient for the corresponding transition. Equation (1) is given here in its standard line-ratio form to illustrate the physical basis of rotational temperature retrieval.

Based on this principle, the Fast Airglow Spectral Line-Ratio Algorithm (FASLR) is developed for temperature retrieval in the mesopause region. Rather than determining temperature by iterative fitting of the full observed spectrum, FASLR uses selected rotational lines in the $O_2$ (0–1) band to construct line-intensity ratios and establishes the corresponding ratio–temperature

relationships from forward-modeled synthetic spectra over a prescribed temperature range, from which multiple ratio-based temperature estimates can be obtained from the observed spectrum.

### 3.2 Temperature retrieval

Figure 2 illustrates the construction of synthetic spectra and the fitted ratio–temperature relationships used for rotational temperature retrieval in the $O_2$ (0–1) band. As shown in Fig. 2a, synthetic concentric-ring images are generated over a prescribed temperature range using a previously developed MASP forward model. This forward model combines spectroscopic parameters from the HITRAN database with atmospheric radiative transfer and the $O_2$ channel instrumental response.

For each temperature, the forward-modeled image is converted into a spectrum by averaging the signal within concentric annuli. The annular mean values are then arranged along the radial coordinate to form a synthetic spectrum. Repeating this procedure over the prescribed temperature range yields a set of synthetic spectra corresponding to different rotational temperatures (Fig. 2b). Within the $O_2$ (0–1) band, the P1(1)–P1(4) lines are selected for temperature retrieval. Among them, P1(3) exhibits the weakest temperature dependence over the considered range and is therefore chosen as the reference line. Three line-intensity ratios, P1(1)/P1(3), P1(2)/P1(3), and P1(3)/P1(4), are then constructed and fitted as functions of temperature over 130–280 K (Fig. 2c).

For a given input spectrum, the peak intensities of P1(1)–P1(4) are extracted to calculate the corresponding line-intensity ratios. Each ratio is then converted to temperature using its fitted ratio–temperature relationship, yielding three separate ratio-based temperature estimates, $T_1$, $T_2$, and $T_3$, corresponding to P1(1)/P1(3), P1(2)/P1(3), and P1(3)/P1(4), respectively. For idealized synthetic spectra generated by the forward model, the three ratios yield temperature estimates consistent with the prescribed temperature. In actual observations, however, the three ratio-based temperature estimates do not necessarily coincide.

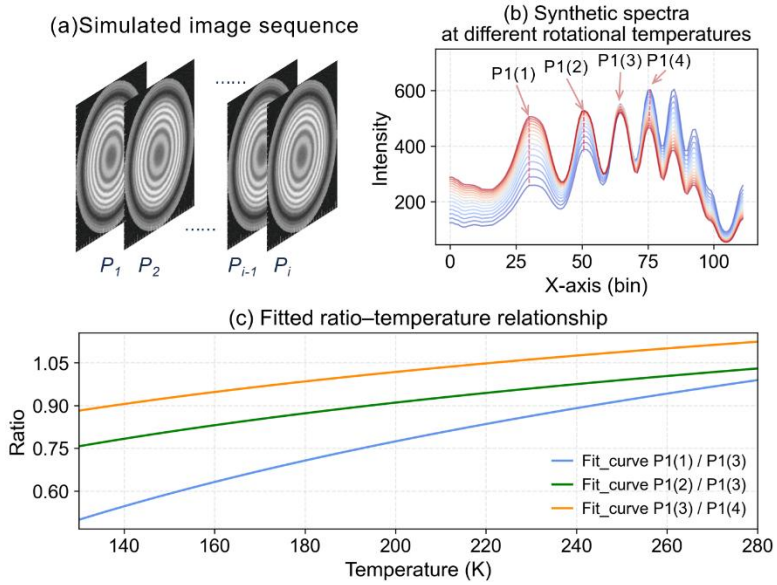



**Figure 2: Construction of the synthetic spectra and fitted ratio–temperature relationships used for $O_2$ (0–1) rotational temperature retrieval. (a) Sequence of simulated concentric-ring images generated over the prescribed temperature range. (b) Synthetic spectra derived from the simulated images by annular averaging, with the P1(1)–P1(4) lines indicated. (c) Quadratic fits of the ratio–temperature relationships for P1(1)/P1(3), P1(2)/P1(3), and P1(3)/P1(4), from which ratio-based temperature estimates are obtained.**

Figure 3 illustrates the different ways in which MPII and FASLR use the observed spectrum for temperature retrieval. MPII uses the spectral profile over the selected range and iteratively adjusts multiple parameters in the forward model to reproduce the observed spectrum. In contrast, FASLR retrieves temperature from selected line-intensity ratios rather than through iterative spectral-profile matching (Fig. 3b).

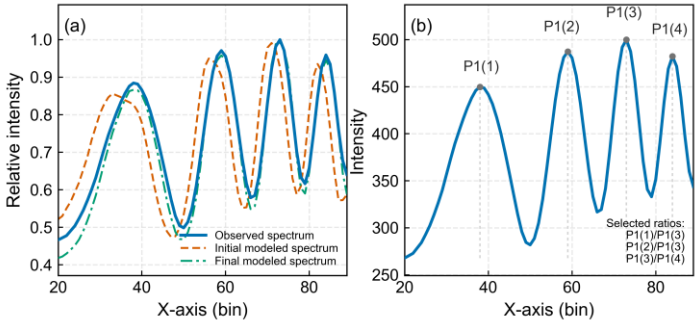



**Figure 3. Illustration of the spectra and line-intensity ratios used by MPII and FASLR for temperature retrieval. (a) Normalized observed spectrum together with the initial and final synthetic spectra used in MPII. (b) Observed spectrum showing the P1(1), P1(2), P1(3), and P1(4) lines selected for the three line-intensity ratios used in FASLR.**

### 3.3 Sensitivity-based weighting

Although FASLR does not iteratively adjust instrumental parameters for each observed spectrum, variations in these parameters can still affect the line intensities and their ratios used for temperature retrieval. To evaluate this effect, the responses of the three selected line-intensity ratios to variations in filter temperature and optical-system focal length were examined using forward-modeled spectra. At a prescribed rotational temperature, variations in filter temperature and optical-system focal length clearly alter the modeled spectral profile (Fig. 4a and 4b). However, the corresponding line-intensity ratios show only limited variations over the prescribed parameter ranges (Fig. 4c and 4d). Figures 4e and 4f further show distinct sensitivity levels among the three ratios, whereas the sensitivity of each individual ratio varies only moderately with rotational temperature over the investigated range. These results indicate that the three ratios have different sensitivities to the instrumental-parameter variations considered here, making it necessary to account for these differences when combining the three ratio-based temperature estimates.

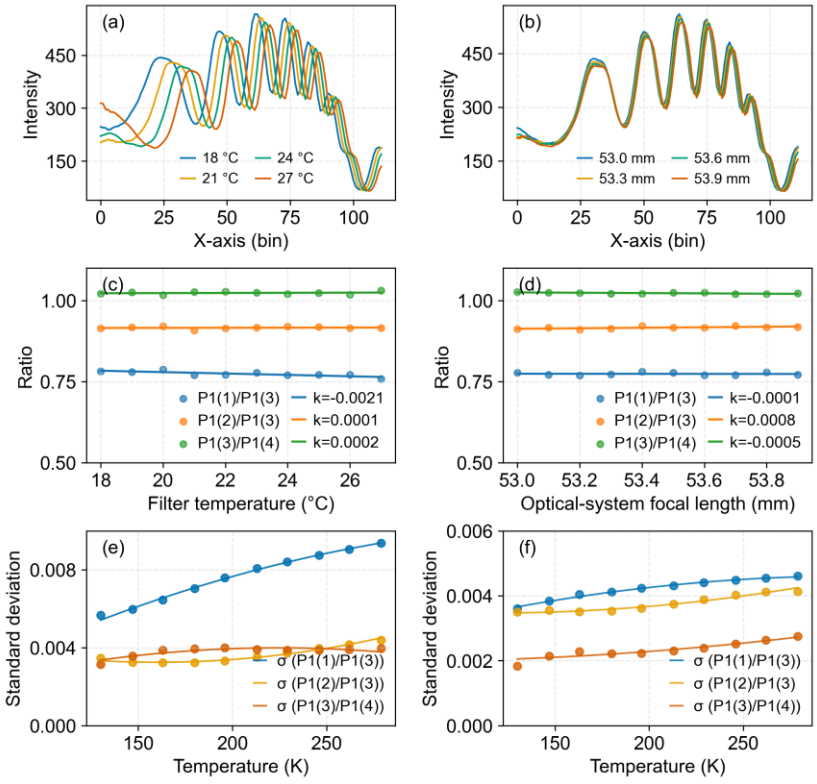


**Figure 4: Sensitivity of the selected line-intensity ratios to instrumental-parameter perturbations. (a) Forward-modeled synthetic spectra at a fixed rotational temperature for different filter temperatures. (b) Same as (a) but for different optical-system focal lengths. (c) Dependence of the three selected line-intensity ratios on filter temperature at the same fixed rotational temperature, with linear fits shown for reference. (d) Same as (c) but for focal-length perturbations. (e) Temperature dependence of the standard deviation of each ratio under filter-temperature perturbations. (f) Same as (e) but for focal-length perturbations.**

A sensitivity-based weighting scheme is therefore used to combine the three ratio-based temperature estimates. The relative contribution of each estimate is determined from the response of the corresponding line-intensity ratio to perturbations in filter temperature and optical-system focal length. Ratios that are less affected by these perturbations are assigned larger weights.

To quantify these responses, single-parameter perturbation tests are performed using forward-modeled synthetic spectra. At each prescribed rotational temperature $T$, the filter temperature $T_f$ is varied over 18–27 °C while the focal length $F$ is held fixed, and $F$ is varied over 53.0–53.9 mm while $T_f$ is held fixed. For the $i$-th ratio $R_i$, the corresponding sensitivities are quantified using the standard deviations of the ratio over the prescribed perturbation ranges:

$$\sigma_i^{(T_f)}(T)=Std\left[R_i\left(T;T_f\right)\right],\quad T_f\in[18,27]℃, \tag{2}$$

$$\sigma_i^{(F)}(T)=Std[R_i(T;F)],\quad F\in[53.0,53.9]mm, \tag{3}$$

where $i$=1,2,3 corresponds to P1(1)/P1(3), P1(2)/P1(3), and P1(3)/P1(4), respectively, and Std is taken over the corresponding perturbation range. These sensitivity measures are evaluated over 130–280 K, and second-order polynomials are fitted to obtain continuous temperature-dependent functions for the two instrumental parameters, as shown in Fig. 4e and 4f.

At each temperature $T$, the sensitivity measures of the three ratios are first normalized separately for the two instrumental parameters:

$$p_i(\mathrm{T})=\frac{\sigma_i^{(T_f)}(\mathrm{T})}{\sum_{j=1}^{3}\sigma_j^{(T_f)}(T)},\qquad q_i(\mathrm{T})=\frac{\sigma_i^{(F)}(T)}{\sum_{j=1}^{3}\sigma_j^{(F)}(T)}. \tag{4}$$

The two normalized sensitivity measures are then combined into a single sensitivity index:

$$r_i(T)=1-\left(1-p_i(T)\right)\left(1-q_i(T)\right), \tag{5}$$

Because $p_i(T)$ and $q_i(T)$ are normalized sensitivity measures bounded between 0 and 1, the combined sensitivity index $r_i(T)$ is also bounded between 0 and 1. A larger $r_i(T)$ indicates a stronger relative response of the $i$-th ratio to the two instrumental-

parameter perturbations considered here. The preliminary weight is defined inversely with respect to the combined sensitivity index:

$$w_i'(T)=\frac{1}{(\varepsilon+r_i(T))}, \tag{6}$$

where $\varepsilon=10^{-6}$ is introduced to avoid division by zero. The three preliminary weights are then normalized at each temperature:

$$w_i(T)=\frac{w_i'(T)}{\Sigma_{j=1}^{3}w_j'(T)}\ . \tag{7}$$

The above calculations yield three temperature-dependent weighting functions, $w_1(T)$、$w_2(T)$ and $w_3(T)$ , as shown in Fig. 5. At any given temperature, the three weights are determined and normalized together, such that their sum equals unity. The weighting is determined only by the sensitivities of the three ratios to the instrumental-parameter perturbations considered here and does not include an additional adjustment based on differences among the individual temperature estimates.

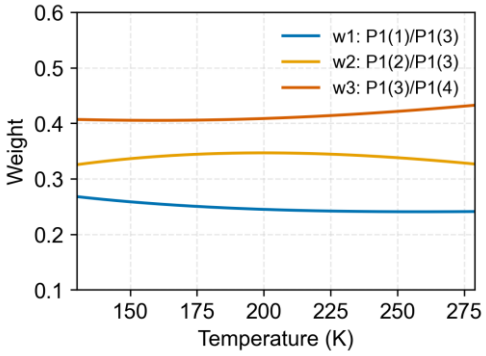



**Figure 5: Temperature-dependent weighting functions used to combine the three ratio-based temperature estimates. The blue, yellow, and orange curves denote the weights assigned to the temperatures derived from P1(1)/P1(3), P1(2)/P1(3), and P1(3)/P1(4), respectively.**

For an actual observation, the three ratio-based temperature estimates $T_1$, $T_2$, and $T_3$ are not necessarily identical. In this study, the three estimates are combined to obtain the final temperature using the temperature-dependent weights derived above. Because the weights vary with temperature, separately selecting $w_1(T_1)$、$w_2(T_2)$ and $w_3(T_3)$ would take the three weights from different normalized weight sets, so their sum would not, in general, equal unity. A common reference temperature $T_{\mathrm{ref}}$ is therefore introduced so that all three weights are evaluated at the same temperature.

In this study, $T_{\mathrm{ref}}$ is defined as the median of the three ratio-based temperature estimates:

$$T_{ref}=\mathrm{median}(T_1, T_2, T_3). \tag{8}$$

The median provides a central value of the three temperature estimates without designating any single ratio as the reference. The three weighting functions are then evaluated at $T_{ref}$, and the final rotational temperature is calculated as:

$$T_{final} = \sum_{i=1}^{3} w_i(T_{ref}) T_i , \quad (9)$$

Here, $T_{ref}$ serves only as a common temperature at which the three temperature-dependent weighting functions are evaluated. To evaluate the influence of $T_{ref}$ on the final result, an additional sensitivity test was performed by perturbing $T_{ref}$ by ±10 and ±20 K while keeping $T_1$, $T_2$, and $T_3$ unchanged. For perturbations of −20 and +20 K, the median absolute changes in $T_{final}$ were 0.017 and 0.027 K, respectively, and 95% of the absolute changes were smaller than 0.049 and 0.072 K, respectively. The changes were still smaller for ±10 K perturbations. These results indicate that the final weighted temperature is only weakly sensitive to variations in $T_{ref}$ within the tested range.

To estimate retrieval uncertainty, the statistical uncertainty of the annularly averaged spectrum was first evaluated at the bins corresponding to the selected line peaks and taken as the statistical uncertainty associated with each line intensity. For each line-intensity ratio, standard error propagation was used to derive the ratio uncertainty, which was then propagated through the fitted ratio-temperature relationship to estimate the uncertainty of the corresponding ratio-based temperature. The uncertainties of the individual ratio-based temperatures were finally combined using the same weights as in the temperature fusion to obtain the estimated uncertainty of each retrieval. The reported uncertainties mainly represent internal retrieval uncertainty derived from statistical error propagation and do not include additional external sources, such as emission-layer altitude variability or representativeness differences.

## 3.4 Practical application and computational characteristics of FASLR

### 3.4.1 Application and comparison with MPII

For retrieval from actual observations, the observed images are first preprocessed to obtain clear concentric-ring patterns with alternating bright and dark fringes, as shown in Fig. 6a. The preprocessing follows Niu et al. (2024), and the ring center is determined using the method of Wei et al. (2023). Using the identified ring center, each image is then converted into a radially averaged spectrum, as shown in Fig. 6b. To reduce the influence of greater random noise in the inner radial bins and stronger

optical-aberration effects in the outer radial bins, the analysis is restricted to radial bin indices 20–80 in the 4 × 4 binned image, which encompass the P1(1)–P1(4) peaks shown in Fig. 6b. The peak intensities of these lines are then extracted to calculate the three line-intensity ratios used in the FASLR retrieval.

Figure 6c presents a representative observation on 23 May 2023. Temperatures retrieved from the three individual line-intensity ratios show clear differences. The temperatures derived from P1(2)/P1(3) are generally higher throughout most of the night, whereas those derived from P1(3)/P1(4) are consistently lower. After sensitivity-based weighting, the FASLR temperatures fall between the three individual retrievals. The FASLR and MPII retrievals show generally similar major temporal variations, including the cooling around 23:30, the recovery after midnight, and the gradual warming during the second half of the night. The estimated retrieval uncertainties of FASLR and MPII are mainly 1.57–2.68 K and 0.50–2.45 K, respectively. Near the end of the observation period, increasing solar contamination degrades the data quality, and the larger differences during this interval are therefore not discussed further.

Figure 6d presents another representative observation on 26 April 2023. The temperatures retrieved from the three individual line-intensity ratios again show clear differences, with the P1(2)/P1(3) retrievals remaining generally higher and the P1(3)/P1(4) retrievals markedly lower for most of the night. The sensitivity-weighted FASLR temperatures again lie between the three individual retrievals and show major temporal variations similar to those of MPII, including the cooling before midnight and the subsequent warming after approximately 01:00. The estimated retrieval uncertainties of FASLR and MPII are mainly 1.41–2.15 K and 1.96–3.56 K, respectively.

For both observation nights, FASLR and MPII show generally similar major temporal variations, although differences remain in their overall temperature levels. In terms of computational performance, the total processing times for the two observation nights were 16.8 and 19.0 s with FASLR, compared with 350.0 and 296.7 s with MPII, respectively. The computational comparison is discussed further in Sect. 3.4.2.

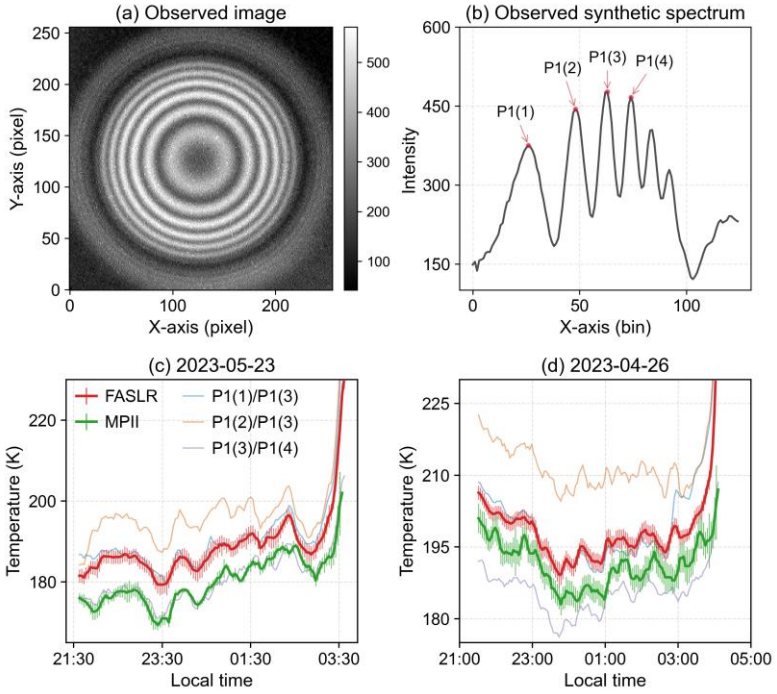



**Figure 6: Practical application of FASLR to $O_2$ (0–1) spectra obtained from single-channel MASP observations in Beijing and comparison with MPII. (a) Preprocessed observed image showing clear concentric-ring fringes. (b) Radially averaged observed spectrum extracted from the image in panel (a), with the $P_1(1)$–$P_1(4)$ peaks marked. Two representative cases showing the temperatures derived from the three selected line-intensity ratios, the final FASLR temperatures after sensitivity-based weighting, and the corresponding MPII results for 23 May 2023 (c) and 26 April 2023 (d), respectively. Error bars denote the estimated retrieval uncertainties of the FASLR and MPII temperatures. The MASP observations were obtained using the original single-channel configuration with a temporal resolution of 3 min.**

### 3.4.2 Computational characteristics and applicability of FASLR

MPII, previously developed for MASP, retrieves rotational temperature by iteratively matching the observed spectrum to forward-modeled spectra. During the iterative retrieval, rotational temperature and instrumental parameters such as filter temperature and optical-system focal length are varied to minimize the spectral mismatch. This procedure requires repeated optimization for each observed spectrum, whereas FASLR directly estimates rotational temperature using line-ratio–temperature relationships derived from forward-modeled spectra.

The computational cost of the two methods was evaluated using the two observation nights shown in Fig. 6. Each method was independently tested 10 times in the same computational environment, with the same preprocessing procedure applied to the

observational data. The timing covered the complete processing workflow from preprocessing of the observational data to generation of the final nightly temperature series. For the 132 observations on 26 April 2023, the mean total processing times were 19.0 s for FASLR and 296.7 s for MPII. For the 120 observations on 23 May 2023, the corresponding times were 16.8 and 350.0 s, respectively. For these two datasets, MPII required approximately 15.6 and 20.8 times the total processing time of FASLR, respectively.

The line-ratio retrieval framework of FASLR is not limited to the $O_2$ (0–1) band considered here. In principle, it can be extended to other airglow bands for which rotational temperature can be derived from suitable line-intensity ratios. In such applications, the band-dependent spectroscopic inputs, channel-specific settings, and selected line ratios need to be adapted, while the general forward-modeling and retrieval framework remains unchanged.

## 4. Comparison of Retrieved Temperatures

### 4.1 Comparison with sodium fluorescence Doppler lidar

Simultaneous MASP and sodium fluorescence Doppler lidar observations were previously conducted, yielding two nights of high-quality coincident data. These observations provide an independent comparison between the temperatures retrieved by FASLR and those measured by the lidar. The observational setting and data processing are described in Sect. 2.2.2.

Figure 7 compares the FASLR and sodium fluorescence Doppler lidar temperatures for the two nights. On both nights, the FASLR temperatures are generally higher than the lidar temperatures. The mean temperature differences over the common observing periods are 8.65 K on 23 May 2023 and 5.38 K on 26 April 2023. To facilitate comparison of the overall nighttime temperature variations between FASLR and the lidar, the nightly mean temperature difference was subtracted from the corresponding FASLR temperature series. The resulting series are shown by the dashed red curves in Fig. 7. The shifted series are included only to facilitate visual comparison of the temporal evolution, while the original FASLR temperatures are retained for comparison of the absolute temperature levels.

As shown in Fig. 7a, the shifted FASLR series and the lidar temperatures on 23 May 2023 show generally similar major temporal variations. Both datasets exhibit the major nocturnal features, including the cooling before midnight and the

subsequent warming later in the night. Some differences remain near the end of the observation period, where increasing solar contamination may reduce the MASP data quality. A similar behavior is found on 26 April 2023 (Fig. 7b). Both datasets show cooling before midnight and subsequent warming after approximately 01:00, although differences remain during some intervals.

Overall, the FASLR and lidar temperatures show generally similar major nocturnal variations on both observation nights, although differences remain in their absolute temperature levels. These comparisons therefore mainly characterize the similarity in temporal evolution between the FASLR and lidar temperatures. A broader assessment of the absolute temperature accuracy of FASLR would benefit from additional simultaneous comparisons with independent temperature measurements over more observation periods.

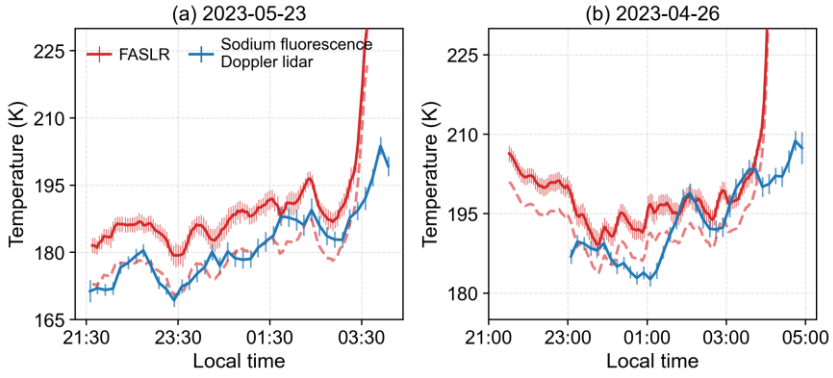



**Figure 7: Comparison of the FASLR and sodium fluorescence Doppler lidar temperatures on (a) 23 May 2023 and (b) 26 April 2023. The solid red curves denote the original FASLR temperatures, the dashed red curves denote the FASLR temperatures after removal of the mean temperature difference relative to the lidar over the common observing period, and the blue curves denote the lidar temperatures. Error bars indicate the corresponding retrieval uncertainties. The dashed curves are included only to facilitate comparison of the temporal evolution between the two datasets and do not represent an absolute correction of the FASLR temperatures.**

### 4.2 Dual-channel observations and intercomparison with multi-source temperatures

#### 4.2.1 Comparison with satellite observations

Figure 8 shows the nocturnal evolution of $O_2$ and OH rotational temperatures retrieved using FASLR during the six observation nights, together with the $O_2$ temperatures retrieved using MPII for comparison. For the OH (6–2) channel, temperatures were

retrieved using the same forward-modeling and line-ratio-based procedure as that used for the $O_2$ (0–1) band, with only the band-specific spectroscopic inputs, channel settings, and selected line ratios adapted. Across the six observation nights, the FASLR and MPII $O_2$ temperatures generally show similar major nocturnal variations. The FASLR $O_2$ rotational temperatures are mainly distributed within 182–212 K, with estimated retrieval uncertainties primarily in the range of 1.7–3.2 K. The FASLR OH rotational temperatures mainly fall within 197–227 K, with estimated retrieval uncertainties primarily in the range of 1.6–3.7 K, and are generally higher than the $O_2$ temperatures. This behavior is consistent with previous airglow observations reported by Sargoytchev et al. (2004).

SABER and Aura/MLS temperatures are also included in Fig. 8 for comparison with the FASLR rotational temperatures. Overall, the available satellite temperatures generally fall within or close to the range of the FASLR retrievals. The available satellite measurements generally show a similar relative temperature difference between the two emission layers. For the available satellite comparisons, SABER temperatures are, on average, about 9.2 K higher than the FASLR temperatures in the OH layer and about 9.7 K higher in the $O_2$ layer. Aura/MLS temperatures are, on average, about 3 K lower than the FASLR temperatures in the OH layer and about 4.7 K higher in the $O_2$ layer. These differences may partly arise from the different sampling characteristics of the satellite and ground-based observations. Satellite measurements provide relatively sparse temporal sampling and do not fully coincide with the MASP observations in time and location, while differences in spatial sampling and vertical representativeness may also affect the comparison.

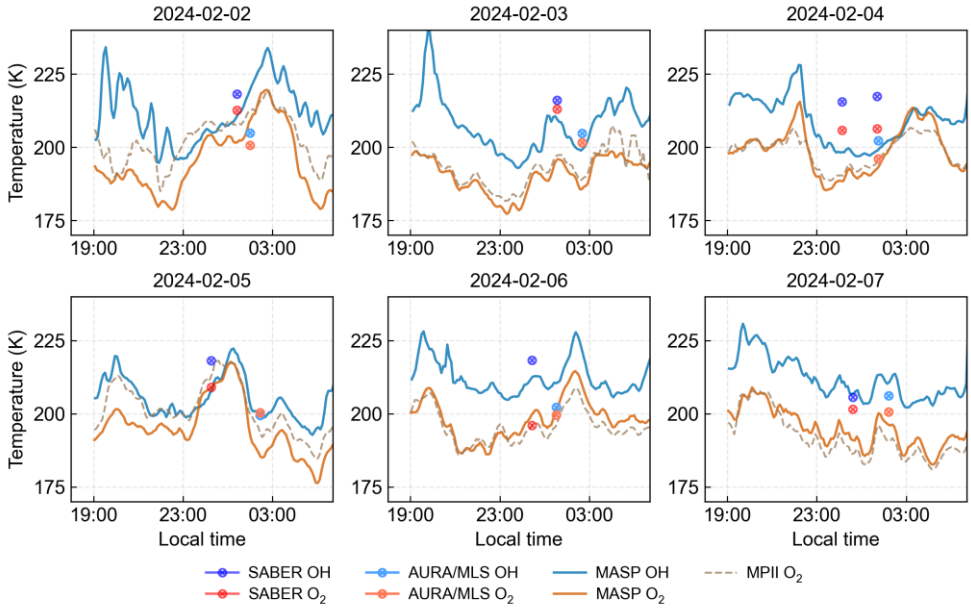



**Figure 8: Rotational temperatures retrieved from the six nights of dual-channel MASP observations and comparison with satellite temperatures. The solid blue and orange curves represent the OH (6–2) and $O_2$ (0–1) rotational temperatures retrieved using FASLR, respectively, while the dashed orange curve represents the corresponding MPII $O_2$ temperatures. The $O_2$ and OH temperature series were obtained from alternating measurements, with an effective temporal resolution of approximately 5.3 min for each channel.**

### 4.2.2 Comparison with SD-WACCMX and NRLMSIS 2.1

Figure 9 shows the composite nocturnal evolution of $O_2$ and OH rotational temperatures retrieved using FASLR, obtained by aligning the six observation nights in local time and calculating the mean temperature at each time stamp. The corresponding MPII $O_2$ temperatures are included for comparison. Temperatures from SD-WACCMX and NRLMSIS 2.1 are also included to examine how the retrieved rotational temperatures relate to the modeled background thermal structure and its slow nocturnal evolution.

Because the model fields have much coarser spatiotemporal resolution than the ground-based observations and differ in spatial and vertical representativeness, the comparison focuses on the background temperature level and slowly varying nocturnal evolution rather than short-term fluctuations.

For $O_2$ (0–1), the FASLR and MPII temperatures show a similar mean nocturnal evolution, with a decrease during the first half of the night followed by an increase after approximately 23:00. NRLMSIS 2.1 remains closer to the retrieved temperatures in overall temperature level during much of the night, although its nocturnal evolution differs from that of FASLR and MPII. In contrast, SD-WACCMX is generally lower than the retrieved $O_2$ temperatures and shows weaker nocturnal variability. Overall, the retrieved and modeled temperatures remain within a comparable nighttime temperature range.

For OH (6–2), the FASLR temperatures are higher than both model estimates during the early part of the night. The difference from NRLMSIS 2.1 decreases as the night progresses, and the FASLR temperatures show a broadly similar nocturnal evolution to NRLMSIS 2.1 during the middle and later parts of the night. In contrast, SD-WACCMX remains generally lower than the retrieved OH temperatures and shows only weak nocturnal variability

The differences between the ground-based OH rotational temperatures and the model temperatures may partly result from differences in vertical representativeness between the airglow measurements and the model temperature fields. Although the model temperatures were averaged over the nominal OH emission altitude range, the effective OH emission height and layer thickness can vary with local time and atmospheric dynamics (Wüst et al., 2023). Previous comparisons between ground-based OH temperatures and profile-derived OH-equivalent temperatures have also shown that variations in OH layer altitude and thickness can affect comparisons based on fixed altitude ranges or climatological weighting functions (Mulligan and Lowe, 2008).

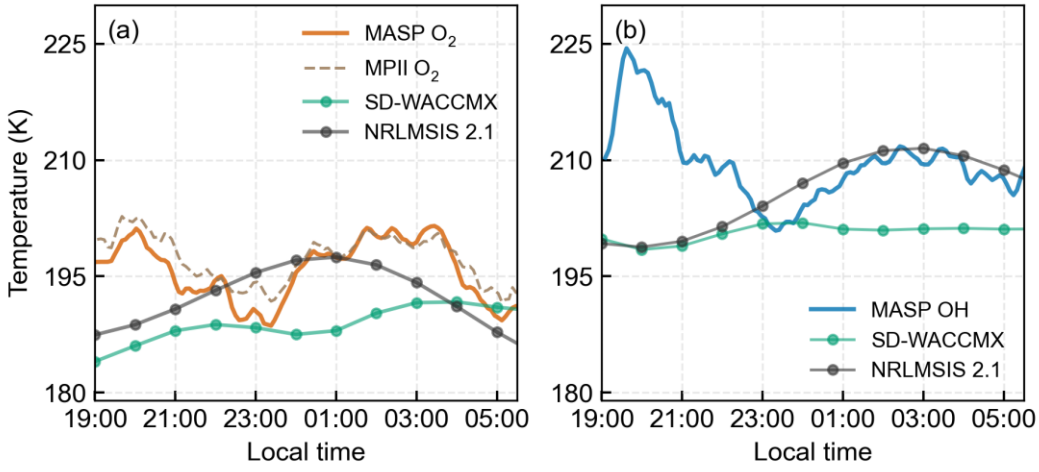


**Figure 9: Composite nocturnal evolution of rotational temperatures from six observation nights and comparison with model temperatures. (a) $O_2$ (0–1) rotational temperature. (b) OH (6–2) rotational temperature. The thick solid orange and blue curves denote the composite mean $O_2$ and OH rotational temperatures retrieved using FASLR, respectively, while the dashed orange curve in (a) denotes the corresponding MPII $O_2$ temperature. The green and black curves represent the corresponding temperatures from SD-WACCMX and NRLMSIS 2.1, respectively.**

## 5. Assessment of FASLR retrievals for wave diagnostics

To evaluate the capability of the FASLR temperature series for identifying wave signatures, the rotational temperature and emission intensity time series derived from the $O_2$ and OH channels were analyzed. Variability on different temporal scales was characterized using two complementary approaches, in which spectral analysis was employed to identify dominant periodic oscillations in the nighttime series, whereas wavelet analysis was applied to detect transient wave activity.

Two representative events from different observation nights are selected for illustration. The first case corresponds to 2 February 2024, when a stable dominant oscillation is observed throughout the night and analyzed using spectral methods. The second case corresponds to 7 February 2024, during which a transient enhancement of wave activity is detected and investigated using wavelet analysis.

### 5.1 Dominant oscillation on 2 February 2024

During the campaign, the effective observing duration for each night was ~10 h. The retrieved temperature time series therefore provides sufficient temporal coverage and resolution to support statistical analyses of whole-night variability. On this basis, consistency analyses of oscillations are performed using the dual-channel rotational temperature $T(t)$ and emission intensity $I(t)$.

The slowly varying nocturnal trend in the temperature and intensity series is removed by second-order polynomial detrending. The residual series are then normalized by the corresponding nightly mean values to obtain the relative perturbations, $\Delta T/T_0$ and $\Delta I/I_0$ , where $T_0$ and I $I_0$ are the nightly mean temperature and intensity, respectively. These normalized perturbation series are subsequently analyzed using Lomb–Scargle analysis to identify the dominant long-period oscillation with periods longer than 6 h (Takahashi et al. 2011). A sinusoidal fit is then performed at the identified period to derive the amplitude, phase, and fit quality, which together characterize the primary features of the whole-night oscillation. Representative nights are identified

by requiring the dominant periods derived from temperature and intensity in both the $O_2$ and OH channels to agree within ±15%, and the corresponding sinusoidal fits to yield correlation coefficients r>0.7.

Among the six nights analyzed, only 2 February 2024 satisfied the above selection criteria and was therefore chosen for detailed analysis. Figure 10 illustrates the representative results for the night of 2 February 2024. Figure 10a and 10b present the $O_2$ and OH temperature series, respectively, while Figure 10c and d show the corresponding $O_2$ and OH emission-intensity series. In each panel, the upper part shows the raw time series together with the fitted second-order polynomial background, whereas the lower part shows the normalized residuals and the sinusoidal fit at the identified dominant period. The dominant periods derived from Fig.10 are 6.93, 6.90, 6.78, and 6.82 h, respectively, and the corresponding fit correlations all exceed 0.85. The fitted periods, amplitudes, phases, and correlation coefficients are summarized in Table 1. These results indicating a common long-period oscillation shared by temperature and intensity in both channels. The ~6.8–6.9 h signal is treated here as a common long-period component. Although tidal effects may contribute to the observed variation, the present single-station analysis does not provide sufficient evidence to attribute it specifically to tidal processes.

Given the common dominant period identified within each emission layer, the Krassovsky parameter, $\eta = |\eta|e^{-i\phi}$, is used to characterize the coupling between temperature and intensity perturbation. Here $|\eta|$ denotes the amplitude ratio of the relative intensity perturbation to the relative temperature perturbation, and $\phi$ represents the phase lag of intensity relative to temperature (Walterscheid et al., 1987; Taylor et al., 1991). In both the $O_2$ and OH layers, the temperature variation leads the intensity variation. In the $O_2$ layer, the temperature phase leads the intensity phase by about 15.4°, corresponding to approximately 17.5 min. In the OH layer, the phase lead is about 17.4°, equivalent to approximately 19.9 min. In addition, $|\eta|$ differs markedly between the two layers, with values of 5.85 for $O_2$ and 2.21 for OH, indicating a clear contrast in the amplitude response of intensity to temperature perturbations between the two emission layers.

Overall, these results show that, in addition to providing stable temperature retrievals, FASLR can support diagnostics of dominant periodicity, sinusoidal characteristics, and temperature–intensity coupling within each emission layer. This demonstrates its suitability for nocturnal airglow variability analysis.

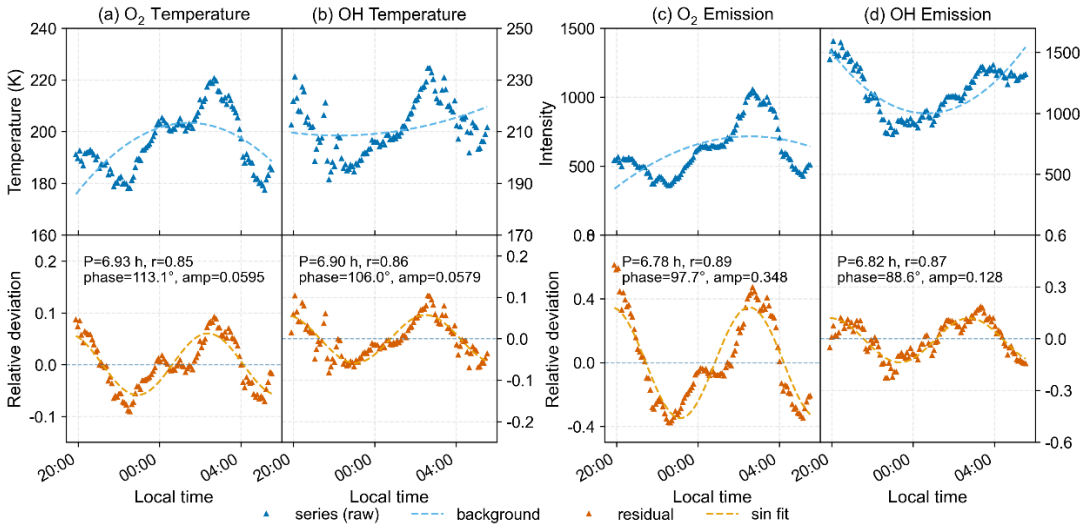



**Figure 10: (a) $O_2$(0-1) temperature series; (b) OH (6-2) temperature series; (c) $O_2$ emission-intensity series; and (d) OH emission-intensity series. Blue triangles denote the raw series, and blue dashed lines denote the slowly varying background trend; orange triangles denote the normalized residuals, and orange dashed lines denote the sinusoidal fits. The labels in each panel indicate the dominant period (P), the correlation coefficient of the sinusoidal fit (r), the fitted phase (in degrees), and the fitted amplitude of the normalized residual series.**

**Table 1. Summary of dominant periods and sinusoidal fitting parameters for the series**

| Layer | Variable | Period(h) | Amplitude | phase (deg) | Correlation coefficient |
|---|---|---|---|---|---|
| $O_2$ | $(T'/T_0)$ | 6.93 | 0.0595 | 113.1 | 0.8457 |
| OH | $(T'/T_0)$ | 6.90 | 0.0579 | 106.0 | 0.8569 |
| $O_2$ | $(I'/I_0)$ | 6.78 | 0.3480 | 97.7 | 0.8936 |
| OH | $(I'/I_0)$ | 6.82 | 0.1280 | 88.6 | 0.8713 |

### 5.2 Short-period disturbance on 7 February 2024

A continuous wavelet transform (CWT) was applied to the $O_2$ and OH rotational temperature and emission-intensity time series to identify short-period disturbances. A representative case occurred on 7 February 2024, when both channels exhibited enhanced short-period variability during the same nighttime interval. For the wavelet analysis, a moving-average method was used to estimate the slowly varying background in the temperature and emission-intensity series, as shown in Fig. 11a–d. The

smoothing window contained 29 points, corresponding to approximately 2.6 h at the effective sampling interval of 5.3 min. The residual series obtained after subtracting the estimated background are presented in Fig. 11e–h and were subsequently used for the continuous wavelet transform.

Figure 11 e–h show that, after removal of the slowly varying background, all four residual series oscillate around zero and exhibit clear quasi-periodic fluctuations. In both emission layers, the temperature residuals are relatively smooth and are reasonably well represented by the sinusoidal fits, whereas the intensity residuals show stronger intermittency and sharper local enhancements. This suggests that the short-period disturbance is present in both temperature and intensity, but with more pronounced non-stationarity in the emission-intensity series. Among the four series, the OH emission-intensity residual is the least regular and is associated with the most diffuse wavelet-power distribution, indicating that its short-period component is less well defined than in the other three series. Nevertheless, its main power enhancement still overlaps in both time and period with the other series, and is therefore interpreted as a weaker but still consistent response to the same short-period disturbance.

The wavelet power spectra in Fig. 11 i–l show enhanced short-period power on 7 February 2024. In Fig. 11 i–k, the dominant power enhancement is concentrated mainly within a common period range of about 1.5–2.2 h and occurs primarily during about 00:00–03:00 LT, although the exact peak period varies somewhat among variables. Compared with the other three series, the OH emission-intensity spectrum is more diffuse, suggesting that its short-period response is modulated by additional variability rather than dominated by a single narrow-band component. Nevertheless, its enhanced power still overlaps partially with the other series in time–period space, supporting the presence of a common short-period disturbance in the two emission layers.

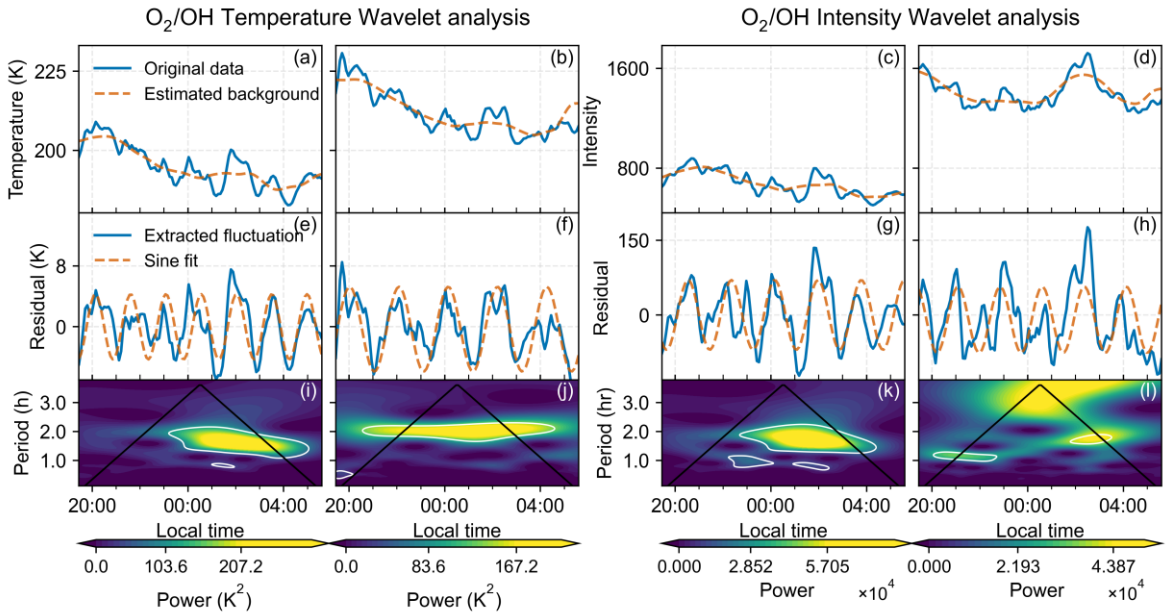



**Figure 11: (a), (b) Original $O_2$ and OH temperature series with the estimated slowly varying background. (c), (d) Original $O_2$ and OH emission-intensity series with the estimated slowly varying background. (e), (f) Residual temperature series after background removal, together with sinusoidal fits. (g), (h) Residual emission-intensity series after background removal, together with sinusoidal fits. (i)- (l) Continuous wavelet power spectra corresponding to panels (e)-(h). The black curves denote the cone of influence, and the white contours indicate the 95% significance level.**

To provide additional context for the short-period disturbance identified from MASP, simultaneous observations from MAWI were also examined. A zenith-centered region with a radius of 8° was selected from the MAWI images, and the median intensity within this region was used to construct a regional intensity time series. As shown in Fig. 12a and 12b, the slowly varying background was estimated using a moving-average method and removed to obtain the fluctuation series. The wavelet power spectrum in Fig. 12c shows enhanced short-period power mainly near 1.4–1.6 h during about 00:00–03:00 LT, overlapping the time interval of the MASP disturbance and partially overlapping its period range. Meanwhile, the corresponding imager frames in Fig. 12d display continuous band-like structures characteristic of gravity-wave activity. These independent observations therefore provide supportive evidence that a short-period gravity-wave disturbance was present during the interval identified from the MASP data.

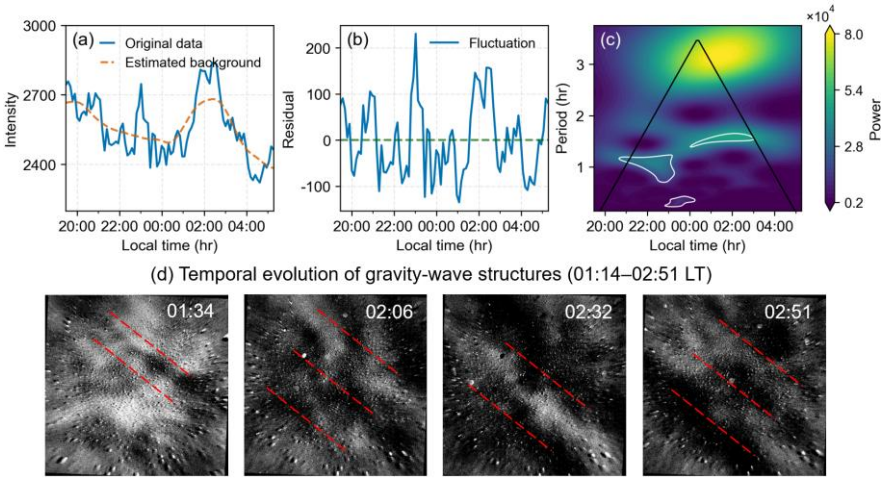



**Figure 12: (a) Zenith-region intensity series and estimated background. (b) Background-removed fluctuation series. (c) Wavelet power spectrum of the fluctuation series (d) Representative imager frames during 01:14–02:51 LT, showing band-like gravity-wave structures. These observations provide independent support for the existence of a short-period gravity-wave disturbance during the MASP event interval.**

## 6. Discussion Conclusions

By establishing ratio–temperature relationships from forward-modeled synthetic spectra and combining multiple ratio-based temperature estimates using sensitivity-based weights, FASLR does not require the per-spectrum iterative optimization used in MPII. This direct retrieval procedure reduces the computational cost of processing continuous airglow observations. The present tests show lower computational cost for FASLR than for MPII, while the temperatures retrieved by the two methods exhibit generally similar major temporal variations. Differences in their overall temperature levels, however, remain and require further evaluation.

Comparison with two nights of simultaneous MASP and sodium fluorescence Doppler lidar observations shows generally similar major nocturnal temperature variations between the two measurements, although differences remain in their absolute temperature levels. FASLR was also applied to dual-channel rotational temperature retrievals for the $O_2$ (0–1) and OH (6–2) emissions. The available SABER and Aura/MLS temperatures were generally within or close to the range of the FASLR retrievals and provided an independent comparison of the temperature levels in the two emission layers. Given differences in sampling and representativeness, the interpretation focuses on these broader features. Comparisons with SD-WACCMX and

NRLMSIS 2.1 show different relationships for the $O_2$ and OH emission layers. At representative emission-layer altitudes, the $O_2$ rotational temperatures are generally in a nighttime temperature range comparable to the model estimates, although their nocturnal variations differ among the datasets. The OH rotational temperatures are higher than both model temperatures during the early part of the night, while the difference from NRLMSIS 2.1 decreases later in the night. SD-WACCMX remains generally lower than the retrieved OH temperatures and shows weaker nocturnal variability. These differences may partly reflect variations in emission-layer altitude and differences in the spatial and vertical representativeness of the ground-based observations and model fields.

Two representative cases further illustrate the use of FASLR-derived temperatures for examining variability on different temporal scales. On 2 February 2024, temperature and intensity perturbations in the $O_2$ and OH emission layers share a common dominant period band and stable phase relationships. The corresponding temperature and intensity perturbations were further used to estimate the Krassovsky parameter. On 7 February 2024, both emission layers exhibit concurrent power enhancements within similar period bands over the same interval, while simultaneous MAWI images reveal coherent banded structures. Together, these cases illustrate the potential of FASLR-derived temperature series for examining both longer-period nocturnal variability and shorter-period disturbances, supporting investigations of multiscale wave processes in the mesopause region. Further efforts may also explore the development and validation of a framework for retrieving two-dimensional temperature-perturbation fields by combining FASLR temperatures with wave-structure information from MAWI image sequences.

**Data availability**

The datasets supporting this study are archived in Zenodo at https://doi.org/10.5281/zenodo.19363272. The deposited materials include the raw dual-channel MASP observations collected during the six nights from 2 to 7 February 2024; the processed temperature comparison data for 26 April 2023 and 23 May 2023, including the FASLR and MPII temperature series and the processed sodium fluorescence Doppler lidar temperature products used in the manuscript; and the representative MAWI image subset directly used in the gravity-wave event analysis presented in this study. The lidar data archived in the repository correspond to the processed temperature products used in this work rather than the original raw measurements. The SD-

WACCMX data used in this study were generated by our group using the WACCM-X model in the specified-dynamics configuration and are available from the corresponding author upon reasonable request. Third-party datasets and model resources used in this work are available from their official sources. TIMED/SABER data were obtained from the SABER Data Services portal. Aura/MLS data were obtained from the official Aura MLS data portal. The NRLMSIS 2.1 model is available through the NASA CCMC access pages. These third-party datasets and model resources are cited accordingly in the manuscript.

**Code availability**

The code used in this study is currently not publicly archived. The main routines for spectral processing and rotational temperature retrieval are available from the corresponding author upon reasonable request.

**Author contributions**

Conceptualization: Shuqi Niu

Formal analysis: Shengyang Gu, Shuqi Niu

Methodology: Shengyang Gu, Shuqi Niu, Haiyang Gao

Resources: Dini Gong, Yafei Wei, Yusong Qin

Validation: Shuqi Niu

Visualization: Shuqi Niu

Writing-original draft: Shuqi Niu

Writing-review & editing: Shengyang Gu

**Competing interests**

The authors declare that they have no conflict of interest.

**Acknowledgements**

This work was supported by the National Natural Science Foundation of China (Grant No. 42374223), the Natural Science Foundation of Wuhan (Grant 2025041001010362), the Fundamental Research Funds for the Central Universities (242025kf0035, 2042025gf0003).

**References**

Brooke, J. S. A., Bernath, P. F., Western, C. M., Sneden, C., Afşar, M., Li, G., and Gordon, I. E.: Line strengths of rovibrational and rotational transitions in the $X^2\Pi$ ground state of OH, J. Quant. Spectrosc. Ra., 168, 142–157, https://doi.org/10.1016/j.jqsrt.2015.07.021, 2016.

Chen, Z., Xu, J., Hu, X., Chen, H., Chen, W., Wei, K., Bian, J., Tian, W., Zhang, S., Ren, R., and Dou, X.: Advances in the researches of the middle and upper atmosphere in China in 2014–2016, Chin. J. Space Sci., 36, 738–752, https://doi.org/10.11728/cjss2016.05.738, 2016.

French, W. J. R., Mulligan, F. J., and Klekociuk, A. R.: Analysis of 24 years of mesopause region OH rotational temperature observations at Davis, Antarctica – Part 1: long-term trends, Atmos. Chem. Phys., 20, 6379–6394, https://doi.org/10.5194/acp-20-6379-2020, 2020.

Shepherd, M. G., Meek, C. E., Hocking, W. K., Hall, C. M., Partamies, N., Sigernes, F., Manson, A. H., and Ward, W. E.: Multi-instrument study of the mesosphere-lower thermosphere dynamics at 80°N during the major SSW in January 2019, J. Atmos. Sol.-Terr. Phys., 210, 105427, https://doi.org/10.1016/j.jastp.2020.105427, 2020.

Stober, G., Kozlovsky, A., Liu, A., Qiao, Z., Tsutsumi, M., Hall, C., Nozawa, S., Lester, M., Belova, E., Kero, J., Espy, P. J., Hibbins, R. E., and Mitchell, N.: Atmospheric tomography using the Nordic Meteor Radar Cluster and Chilean Observation Network De Meteor Radars: network details and 3D-Var retrieval, Atmos. Meas. Tech., 14, 6509–6532, https://doi.org/10.5194/amt-14-6509-2021, 2021.

Yang, Y., Li, F., Cheng, X., Yang, G., Lyu, D., Lin, X., Liu, L., Fang, X., Zheng, J., Du, L., Wang, W., Ren, L., Wang, J., Liang, J., Ji, K., Xu, L., Chen, Z., Ji, K., Zheng, H., Wang, X., Wang, Y., Jiao, J., Wang, X., Xue, X., Xia, Y., Li, Y., Lin, Z.,

Chen, L., Chen, Z., Xu, J., Li, G., Hu, L., and Gong, S.: Lidar Network for Temperature and Wind Measurements in the Mesosphere and Lower Thermosphere Region, Space Weather, 22, e2024SW003981, https://doi.org/10.1029/2024SW003981, 2024.

Huang, H., Gu, S.-Y., Qin, Y., Li, G., Yang, Z., Wei, Y., Gong, D., and Niu, S.: Statistical analysis of gravity waves in the mesopause region based on OI 557.7 nm airglow observation over Mohe, China, J. Geophys. Res.-Space, 130, e2025JA033917, https://doi.org/10.1029/2025JA033917, 2025.

Li, T., Leblanc, T., McDermid, I. S., Wu, D. L., Dou, X. K., and Wang, S.: Seasonal and interannual variability of gravity wave activity revealed by long-term lidar observations over Mauna Loa Observatory, Hawaii, J. Geophys. Res.-Atmos., 115, D13103, https://doi.org/10.1029/2009JD013586, 2010.

Liu, W., Xu, J., Smith, A. K., and Yuan, W.: Comparison of rotational temperature derived from ground-based OH airglow observations with TIMED/SABER to evaluate the Einstein coefficients, J. Geophys. Res.-Space, 120, 10069–10082, https://doi.org/10.1002/2015JA021886, 2015.

López-González, M.J., García-Comas, M., Rodríguez, E., López-Puertas, M., Shepherd, M.G., Shepherd, G.G., Sargoytchev, S., Aushev, V.M., Smith, S.M., Mlynczak, M.G., Russell, J.M., Brown, S., Cho, Y., and Wiens, R.H.: Ground-based mesospheric temperatures at mid-latitude derived from $O_2$ and OH airglow SATI data: Comparison with SABER measurements, J. Atmos. Sol.-Terr. Phy., 69, 2379–2390, https://doi.org/10.1016/j.jastp.2007.07.004, 2007.

Mies, F. H.: Calculated vibrational transition probabilities of OH($X^2\Pi$), J. Mol. Spectrosc., 53, 150–188, https://doi.org/10.1016/0022-2852(74)90125-8, 1974.

Mulligan, F. J. and Lowe, R. P.: OH-equivalent temperatures derived from ACE-FTS and SABER temperature profiles – a comparison with OH*(3–1) temperatures from Maynooth (53.2° N, 6.4° W), Ann. Geophys., 26, 795–811, https://doi.org/10.5194/angeo-26-795-2008, 2008.

Mulligan, F. J., Dyrland, M. E., Sigernes, F., and Deehr, C. S.: Inferring hydroxyl layer peak heights from ground-based measurements of OH (6–2) band integrated emission rate at Longyearbyen (78° N, 16° E), Ann. Geophys., 27, 4197–4205, https://doi.org/10.5194/angeo-27-4197-2009, 2009.

Niu, S., Gao, H., Yan, Z., Ren, K., Kou, L., Jiang, B., and Bu, L.: High-precision temperature retrieval algorithm and verification for mesospheric airglow spectrum photometer, Sci. China Earth Sci., 67, 1639–1651, https://doi.org/10.1007/s11430-023-1298-y, 2024.

Noll, S., Kausch, W., Kimeswenger, S., Unterguggenberger, S., and Jones, A. M.: Comparison of VLT/X-shooter OH and $O_2$ rotational temperatures with consideration of TIMED/SABER emission and temperature profiles, Atmos. Chem. Phys., 16, 5021–5042, https://doi.org/10.5194/acp-16-5021-2016, 2016.

Noll, S., Schmidt, C., Kausch, W., Bittner, M., and Kimeswenger, S.: Climatologies of Various OH Lines From About 90,000 X-Shooter Spectra, J. Geophys. Res.-Atmos., 128, e2022JD038275, https://doi.org/10.1029/2022JD038275, 2023.

Osterbrock, D. E., Fulbright, J. P., Martel, A. R., Keane, M. J., Trager, S. C., and Basri, G.: Night-sky high-resolution spectral atlas of OH and $O_2$ emission lines for echelle spectrograph wavelength calibration, Publ. Astron. Soc. Pac., 108, 277–308, https://doi.org/10.1086/133722, 1996.

Reisin, E. R., Scheer, J., Dyrland, M. E., Sigernes, F., Deehr, C. S., Schmidt, C., Höppner, K., Bittner, M., Ammosov, P. P., Gavrilyeva, G. A., Stegman, J., Perminov, V. I., Semenov, A. I., Knieling, P., Koppmann, R., Shiokawa, K., Lowe, R. P., López-González, M. J., Rodríguez, E., Zhao, Y., Taylor, M. J., Buriti, R. A., Espy, P. J., French, W. J. R., Eichmann, K.-U., Burrows, J. P., and von Savigny, C.: Traveling planetary wave activity from mesopause region airglow temperatures determined by the Network for the Detection of Mesospheric Change (NDMC), J. Atmos. Sol.-Terr. Phy., 119, 71–82, https://doi.org/10.1016/j.jastp.2014.07.002, 2014.

Sargoytchev, S. I., Brown, S., Solheim, B. H., Cho, Y.-M., Shepherd, G. G., and López-González, M. J.: Spectral airglow temperature imager (SATI): a ground-based instrument for the monitoring of mesosphere temperature, Appl. Opt., 43, 5712–5721, https://doi.org/10.1364/AO.43.005712, 2004.

Shepherd, G. G., Hagan, M., and Portnyagin, Y.: PSMOS 2000 workshop – planetary scale mesopause observing system, J. Atmos. Sol.-Terr. Phy., 64, 873–874, https://doi.org/10.1016/S1364-6826(02)00038-X, 2002.

Sigernes, F., Shumilov, N., Deehr, C. S., Nielsen, K. P., Svenøe, T., and Havnes, O.: Hydroxyl rotational temperature record from the auroral station in Adventdalen, Svalbard (78° N, 15° E), J. Geophys. Res.-Space, 108, 1342, https://doi.org/10.1029/2001JA009023, 2003.

Sun, K., Yousefi, M., Chan Miller, C., Chance, K., González Abad, G., Gordon, I. E., Liu, X., O'Sullivan, E., Sioris, C. E., and Wofsy, S. C.: An optimal estimation-based retrieval of upper atmospheric oxygen airglow and temperature from SCIAMACHY limb observations, Atmos. Meas. Tech., 15, 3721–3745, https://doi.org/10.5194/amt-15-3721-2022, 2022.

Takahashi, H., Onohara, A., Shiokawa, K., Vargas, F., and Gobbi, D.: Atmospheric wave induced $O_2$ and OH airglow intensity variations: effect of vertical wavelength and damping, Ann. Geophys., 29, 631–637, https://doi.org/10.5194/angeo-29-631-2011, 2011.

Takeuchi, I. and Misawa, K.: Successive approximation for determining the hydroxyl rotational temperature, Appl. Opt., 18, 3805–3809, https://doi.org/10.1364/AO.18.003805, 1979.

Takeuchi, I., Misawa, K., Kato, Y., and Aoyama, I.: Rotational temperatures and intensities of OH(6–2) and OH(8–3) bands in the night airglow, J. Atmos. Terr. Phys., 41, 387–395, https://doi.org/10.1016/0021-9169(79)90035-7, 1979.

Taylor, M. J., Espy, P. J., Baker, D. J., Sica, R. J., Neal, P. C., and Pendleton Jr., W. R.: Simultaneous intensity, temperature and imaging measurements of short period wave structure in the OH nightglow emission, Planet. Space Sci., 39, 1171–1188, https://doi.org/10.1016/0032-0633(91)90169-B, 1991.

Walterscheid, R. L., Schubert, G., and Straus, J. M.: A dynamical-chemical model of wave-driven fluctuations in the OH nightglow, J. Geophys. Res., 92, 1241–1254, https://doi.org/10.1029/JA092iA02p01241, 1987.

Wan, W. and Xu, J.: Recent investigation on the coupling between the ionosphere and upper atmosphere, Sci. China Earth Sci., 57, 1995–2012, https://doi.org/10.1007/s11430-014-4923-3, 2014.

Wang, J., Yi, W., Wu, J., Chen, T., Xue, X., Zeng, J., Vincent, R. A., Reid, I. M., Batista, P. P., Buriti, R. A., Tsuda, T., Mitchell, N. J., and Dou, X.: Coordinated observations of migrating tides by multiple meteor radars in the equatorial mesosphere and lower thermosphere, J. Geophys. Res.-Space, 127, e2022JA030678, https://doi.org/10.1029/2022JA030678, 2022.

Wei, Y., Gu, S.-Y., Yang, Z., Huang, C., Li, N., Hu, G., and Dou, X.: Inversion of wind and temperature from low SNR FPI interferograms, Remote Sens., 15, 1934, https://doi.org/10.3390/rs15071934, 2023.

Wüst, S., Bittner, M., Espy, P. J., French, W. J. R., and Mulligan, F. J.: Hydroxyl airglow observations for investigating atmospheric dynamics: results and challenges, Atmos. Chem. Phys., 23, 1599–1618, https://doi.org/10.5194/acp-23-1599-2023, 2023.

Xiong, J., Wan, W. X., Ning, B., Liu, L., Wu, B., Hu, L., and Xu, T.: Seasonal variations of night mesopause temperature in Beijing observed by SATI4, Sci. China Technol. Sci., 55, 1295–1301, https://doi.org/10.1007/s11431-012-4779-8, 2012.

Xu, J., Li, Q., Yue, J., Hoffmann, L., Straka III, W. C., Wang, C., Liu, M., Yuan, W., Han, S., Miller, S. D., Sun, L., Liu, X., Liu, W., Yang, J., and Ning, B.: Concentric gravity waves over northern China observed by an airglow imager network and satellites, J. Geophys. Res.-Atmos., 120, 11058–11078, https://doi.org/10.1002/2015JD023786, 2015.

Yi, W., Xue, X., Lu, M., Zeng, J., Ye, H., Wu, J., Wang, C., and Chen, T..: Mesopause temperatures and relative densities at midlatitudes observed by the Mengcheng meteor radar, Earth Planet. Phys., 7, 665–674, https://doi.org/10.26464/epp2023083, 2023.

Yue, J., Russell III, J., Jian, Y., Rezac, L., Garcia, R, López-Puertas, M., and Mlynczak, M. G.: Increasing carbon dioxide concentration in the upper atmosphere observed by SABER, Geophys. Res. Lett., 42, 7194–7199, https://doi.org/10.1002/2015GL064696, 2015.